Online Resource 1

Supplementary figures and tables

Article: *Adult neurogenesis promotes pattern separation and sparsity beyond the dentate gyrus in a spiking DG–CA3 model*

Journal: Cognitive Neurodynamics

Authors: Marlon Valmórbida Cendron, Wilfredo Blanco Figuerola, Flávio Freitas Barbosa

Corresponding author: Marlon Valmórbida Cendron, Laboratory for Memory and Cognition Studies, Department of Psychology, Federal University of Paraíba, João Pessoa, Brazil. E-mail: marlonvcendron@gmail.com

Cell	*In Vivo* Firing Rate (Hz)	Reference	Model Firing Rate (Hz)	*In Vivo* Activation	Reference	Model Activation
Mature granule	1.2 (0.56–2.38)	McHugh et al. (2022)	1.08	2–5%	Galloni et al. (2022); Hainmueller and Bartos (2018)	8.0%
	0.49	Diamantaki et al. (2016)		9%	GoodSmith et al. (2017)	
	0.031 ± 0.096	Zhang et al. (2020)				
	0.4	Wheeler et al. (2024)				
	0.96 ± 0.19	GoodSmith et al. (2019)				
	≈ 0.2	Senzai and Buzsáki (2016)				
	$72 \pm 8^{\text{max}}$	Lübke et al. (1998)				
Immature granule	2.3 (1.6–6.7)	McHugh et al. (2022)	2.96			63.8%
Mossy	0.84	Wheeler et al. (2024)	3.45	$\approx 100\%$	Danielson et al. (2017)	96.7%
	1.05 ± 0.07	GoodSmith et al. (2019)		88%	GoodSmith et al. (2017)	
	≈ 0.8	Senzai and Buzsáki (2016)				
	$50 \pm 6^{\text{max}}$	Lübke et al. (1998)				
HIPP	$111.4 \pm 10.2^{\text{max}}$	Yuan et al. (2017)	6.38			100%
Basket	13.6 ± 0.8	Li et al. (2022)	17.35			100%
	$230 \pm 15^{\text{max}}$	Lübke et al. (1998)				
CA3 pyramidal	0.2	Mizuseki and Buzsáki (2013)	1.17	29%	GoodSmith et al. (2017)	30.0%
	0.5	Kay et al. (2016)		20–30%	Galloni et al. (2022)	
	0.72 ± 0.51	Lasztóczi et al. (2011)				
	CA3a: 0.4; CA3b: 0.3	Oliva et al. (2016)				
	1.2	McHugh et al. (2022)				
	0.92 ± 0.06	GoodSmith et al. (2019)				
	≈ 0.6	Senzai and Buzsáki (2016)				
CA3 inhibitory	20 ± 7	Tukker et al. (2013)	6.51			65.4%
	17 ± 7	Lapray et al. (2012)				
	8.2 ± 5.6	Leão et al. (2012)				

Table S1: *In vivo* firing rates and activation (the fraction of active cells) for each cell type, alongside model values. *In vivo* firing rates are mean ± SD. $^{\text{max}}$ maximum firing rate evoked by depolarizing current injection *in vitro* (mean ± SEM for the HIPP cells). ≈ approximate value read from figure. Model firing rates are the mean over active cells and model activation the fraction of active cells; both are from the control network, except the immature granule cells (absent in the control), which are from the neurogenesis model at 50% EC→iGC excitability.

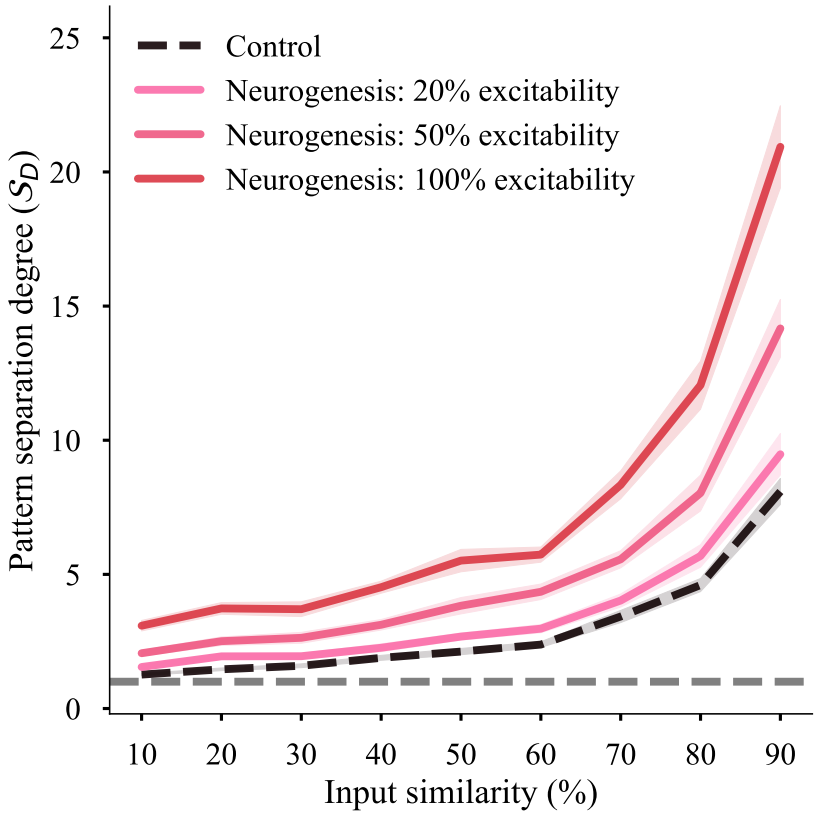

Figure S1: Pattern separation of the mature granule cells resolved by input similarity. Each curve shows the pattern separation degree $\mathcal{S}_D$ of the mGC population as a function of the similarity between the input patterns, for the control network without neurogenesis (black dashed line) and for neurogenesis networks at representative EC→iGC excitability levels. Each point is the mean over the 30 pattern sets and the shaded band shows the standard error of the mean. The grey dashed line marks $\mathcal{S}_D = 1$, above which the output patterns are more distinct than their inputs. Separation is strongest for the most similar (most overlapping) inputs, and every neurogenesis network separates better than the control across the whole similarity range.

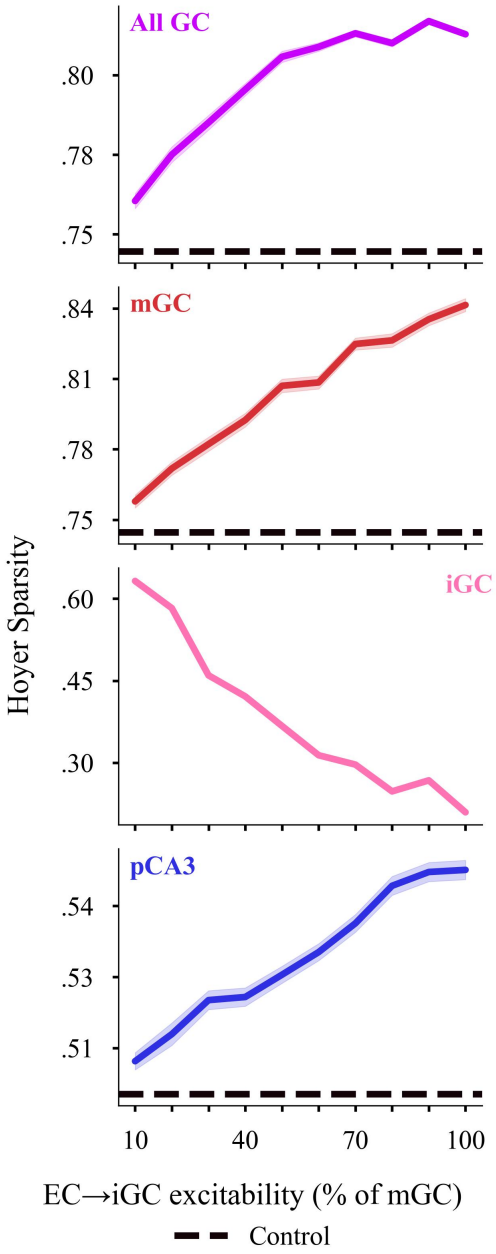

Figure S2: Population sparsity measured with the Hoyer index, as a cross-validation of the Gini results reported in the main text. Each panel shows the Hoyer sparsity of one population, the whole granule-cell population (All GC), the mature granule cells (mGC), the immature granule cells (iGC) and the pyramidal CA3 cells (pCA3), as a function of the EC→iGC excitability level; the shaded bands show the standard error of the mean and the dashed line marks the control network without neurogenesis (absent for the iGC panel, which has no counterpart in the control). As with the Gini index, the sparsity of the All GC, mGC and pCA3 populations rises with iGC excitability and stays above the control, whereas the iGC population becomes less sparse.

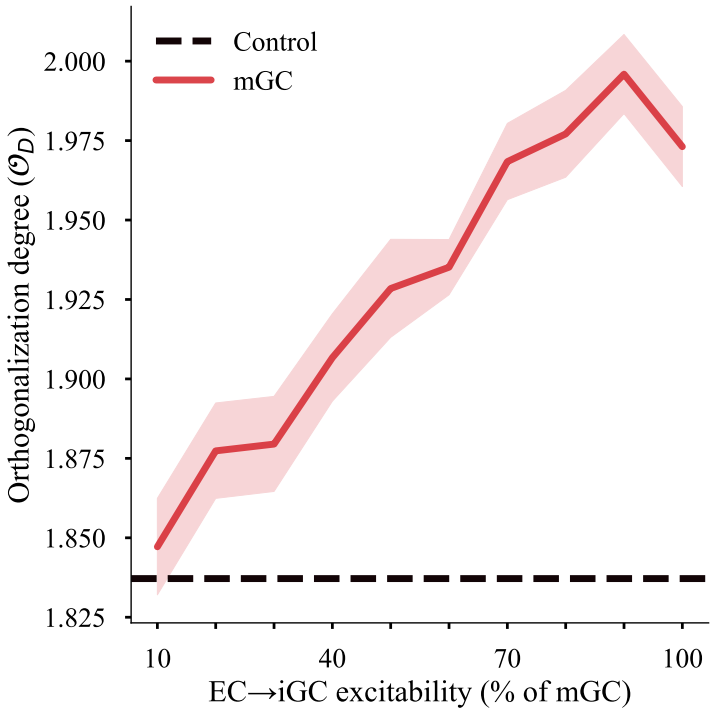

Figure S3: Orthogonalization of the mature granule-cell output as a function of EC→iGC excitability. The curve shows the orthogonalization degree $\mathcal{O}_D$ of the mGC population, taken as the ratio of the output to the input orthogonalization ($O^{(out)}/O^{(in)}$); the shaded band shows the standard error of the mean and the dashed line marks the control network without neurogenesis. The orthogonalization rises with iGC excitability, indicating that the mGC outputs become increasingly decorrelated as neurogenesis increases, beyond what the reduction in the number of active cells alone would produce.

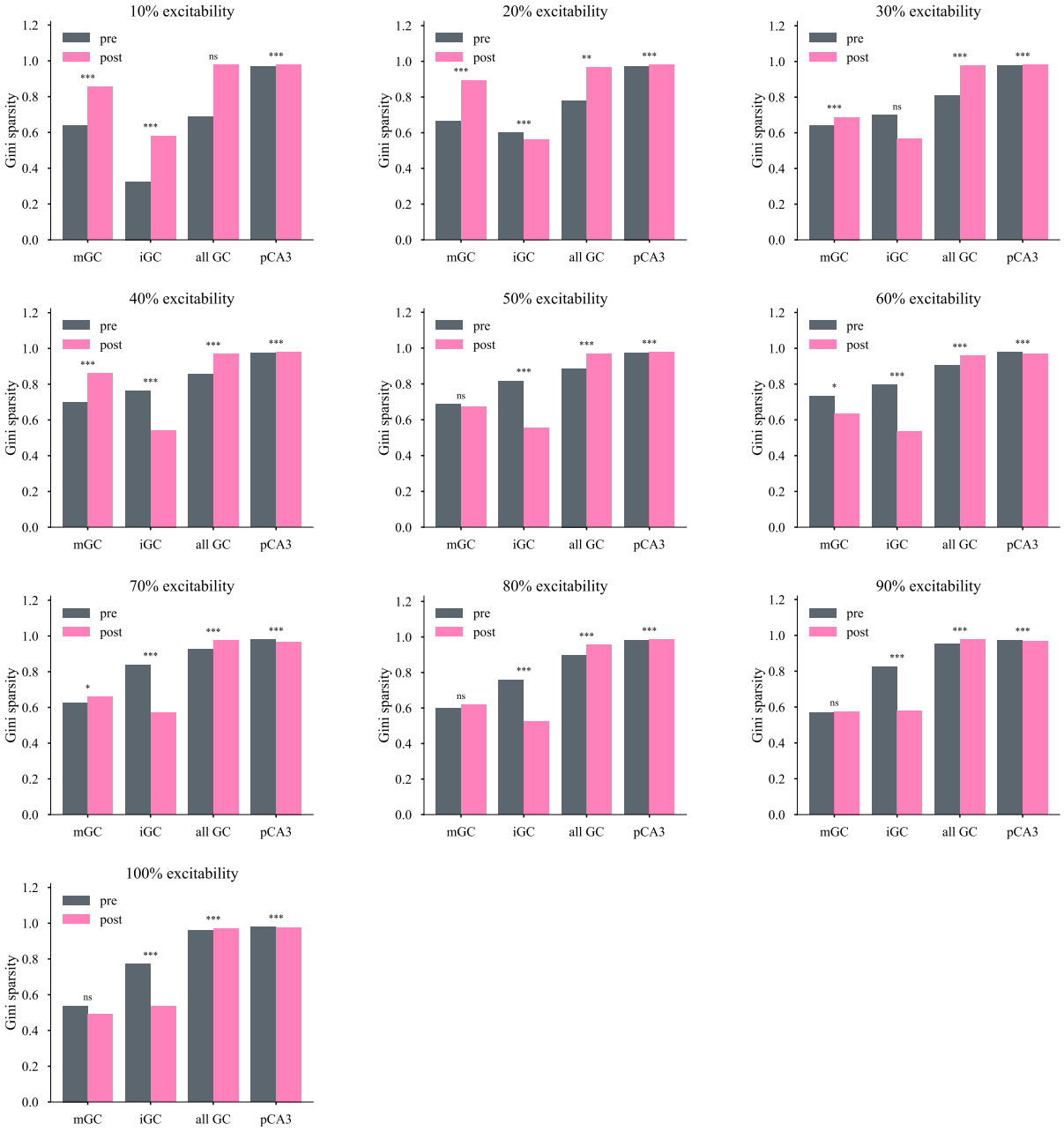

Figure S4: Population sparsity (Gini index) immediately before and after direct iGC activation, for every EC→iGC excitability level. Each panel corresponds to one excitability level (10%–100%, given in the panel title) and compares the Gini index of the mGC, iGC, combined granule-cell (all GC) and pCA3 populations in the 50 ms windows immediately before (pre) and after (post) the depolarizing pulse, pooled over all runs. Bars show the mean across runs. The result of the paired Wilcoxon signed-rank test between the pre and post values is indicated above each pair (ns, not significant; * $p < 0.05$; ** $p < 0.01$; *** $p < 0.001$).

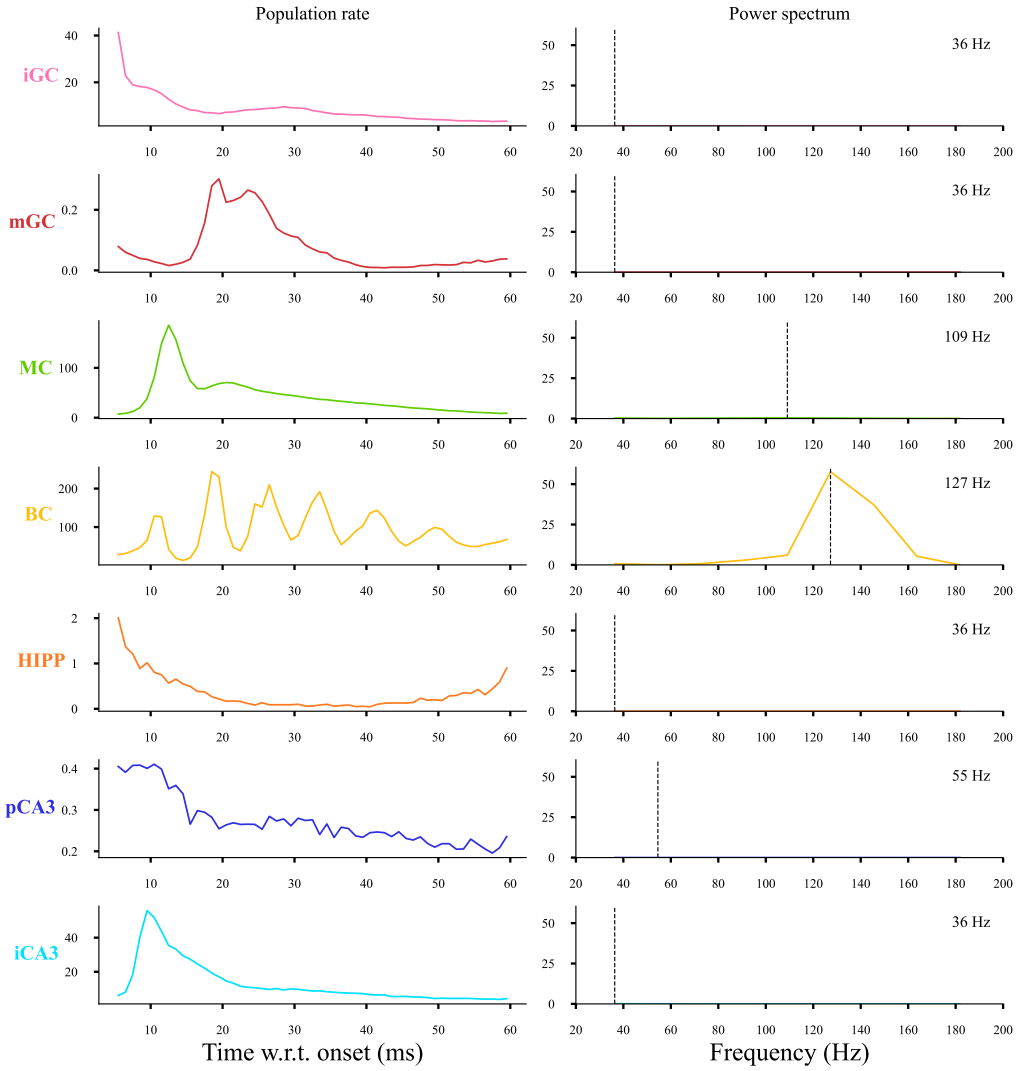

Figure S5: Rhythmicity of the post-pulse response of each population. Left column, population firing rate over the 5 ms to 60 ms window following the onset of the depolarizing pulse delivered to half of the iGCs, pooled over all EC→iGC excitability levels and all runs. Right column, power spectrum of the same signal after subtraction of a Gaussian-smoothed envelope, estimated by Welch's method over the 20 Hz to 200 Hz band; the dashed line and the label mark the peak frequency. Only the BCs show a spectral peak that stands out from the background of their own spectrum, at the frequency reported in the main text; the peak of the MCs carries a power close to the median of their band and the remaining populations peak at the lower edge of the band. The 55 ms analysis window sets the frequency resolution at 18 Hz, so the peak frequencies are accurate only to within one bin.

References

Danielson NB, Turi GF, Ladow M, et al (2017) In Vivo Imaging of Dentate Gyrus Mossy Cells in Behaving Mice. Neuron 93(3):552–559.e4. https://doi.org/10.1016/j.neuron.2016.12.019

Diamantaki M, Frey M, Berens P, et al (2016) Sparse activity of identified dentate granule cells during spatial exploration. eLife 5:e20252. https://doi.org/10.7554/eLife.20252

Galloni AR, Samadzelkava A, Hiremath K, et al (2022) Recurrent Excitatory Feedback From

Mossy Cells Enhances Sparsity and Pattern Separation in the Dentate Gyrus via Indirect Feedback Inhibition. Frontiers in Computational Neuroscience 16:826278. https://doi.org/10.3389/fncom.2022.826278

GoodSmith D, Chen X, Wang C, et al (2017) Spatial Representations of Granule Cells and Mossy Cells of the Dentate Gyrus. Neuron 93(3):677–690.e5. https://doi.org/10.1016/j.neuron.2016.12.026

GoodSmith D, Lee H, Neunuebel JP, et al (2019) Dentate Gyrus Mossy Cells Share a Role in Pattern Separation with Dentate Granule Cells and Proximal CA3 Pyramidal Cells. The Journal of Neuroscience 39(48):9570–9584. https://doi.org/10.1523/JNEUROSCI.0940-19.2019

Hainmueller T, Bartos M (2018) Parallel emergence of stable and dynamic memory engrams in the hippocampus. Nature 558(7709):292–296. https://doi.org/10.1038/s41586-018-0191-2

Kay K, Sosa M, Chung JE, et al (2016) A hippocampal network for spatial coding during immobility and sleep. Nature 531(7593):185–190. https://doi.org/10.1038/nature17144

Lapray D, Lasztoczi B, Lagler M, et al (2012) Behavior-dependent specialization of identified hippocampal interneurons. Nature Neuroscience 15(9):1265–1271. https://doi.org/10.1038/nn.3176

Lasztóczi B, Tukker JJ, Somogyi P, et al (2011) Terminal Field and Firing Selectivity of Cholecystokinin-Expressing Interneurons in the Hippocampal CA3 Area. The Journal of Neuroscience 31(49):18073–18093. https://doi.org/10.1523/JNEUROSCI.3573-11.2011

Leão RN, Mikulovic S, Leão KE, et al (2012) OLM interneurons differentially modulate CA3 and entorhinal inputs to hippocampal CA1 neurons. Nature Neuroscience 15(11):1524–1530. https://doi.org/10.1038/nn.3235

Li R, Zhang W, Zhang J, et al (2022) Sustained Activity of Hippocampal Parvalbumin-Expressing Interneurons Supports Trace Eyeblink Conditioning in Mice. The Journal of Neuroscience 42(44):8343–8360. https://doi.org/10.1523/JNEUROSCI.0834-22.2022

Lübke J, Frotscher M, Spruston N (1998) Specialized Electrophysiological Properties of Anatomically Identified Neurons in the Hilar Region of the Rat Fascia Dentata. Journal of Neurophysiology 79(3):1518–1534. https://doi.org/10.1152/jn.1998.79.3.1518

McHugh SB, Lopes-dos-Santos V, Gava GP, et al (2022) Adult-born dentate granule cells promote hippocampal population sparsity. Nature Neuroscience 25(11):1481–1491. https://doi.org/10.1038/s41593-022-01176-5

Mizuseki K, Buzsáki G (2013) Preconfigured, Skewed Distribution of Firing Rates in the Hippocampus and Entorhinal Cortex. Cell Reports 4(5):1010–1021. https://doi.org/10.1016/j.celrep.2013.07.039

Oliva A, Fernández-Ruiz A, Buzsáki G, et al (2016) Role of Hippocampal CA2 Region in Triggering Sharp-Wave Ripples. Neuron 91(6):1342–1355. https://doi.org/10.1016/j.neuron.2016.08.008

Senzai Y, Buzsáki G (2016) Extracellular recordings of dentate granule cells, mossy cells and CA3 neurons during spatial navigation and sleep in mice. CRCNS.org, https://doi.org/10.6080/K0VX0DFT

Tukker JJ, Lasztóczi B, Katona L, et al (2013) Distinct Dendritic Arborization and *In Vivo* Firing Patterns of Parvalbumin-Expressing Basket Cells in the Hippocampal Area CA3. The Journal of Neuroscience 33(16):6809–6825. https://doi.org/10.1523/JNEUROSCI.5052-12.2013

Wheeler DW, Kopsick JD, Sutton N, et al (2024) Hippocampome.org 2.0 is a knowledge base enabling data-driven spiking neural network simulations of rodent hippocampal circuits. eLife 12:RP90597. https://doi.org/10.7554/eLife.90597

Yuan M, Meyer T, Benkowitz C, et al (2017) Somatostatin-positive interneurons in the dentate gyrus of mice provide local- and long-range septal synaptic inhibition. eLife 6:e21105. https://doi.org/10.7554/eLife.21105

Zhang X, Schlögl A, Jonas P (2020) Selective Routing of Spatial Information Flow from Input to Output in Hippocampal Granule Cells. Neuron 107(6):1212–1225.e7. https://doi.org/10.1016/j.neuron.2020.07.006